



OPEN

Confocal microscopic oxygen imaging of xenograft tumors using Ir(III) complexes as *in vivo* intravascular and intracellular probes

Toshitada Yoshihara¹✉, Takuto Tamura¹, Shuichi Shiozaki¹, Li-Chieh Chou¹, Ryohei Kakuchi¹ & Susumu Rokudai²

Hypoxia is an important feature of the tumor microenvironment (TME) of most solid tumors, and it is closely linked to cancer cell proliferation, therapy resistance, and the tumor immune response. Herein, we describe a method for hypoxia-induced heterogeneous oxygen distribution in xenograft tumors based on phosphorescence imaging microscopy (PLIM) using intravascular and intracellular oxygen probes. We synthesized Ir(III) complexes with polyethylene glycol (PEG) units of different molecular weights into the ligand as intravascular oxygen probes, BTP-PEGm ($m = 2000, 5000, 10000, 20000$). BTP-PEGm showed red emission with relatively high emission quantum yield and high oxygen sensitivity in saline. Cellular and *in vivo* experiments using these complexes revealed that BTP-PEG10000 was the most suitable probe in terms of blood retention and ease of intravenous administration in mice. PLIM measurements of xenograft tumors in mice treated with BTP-PEG10000 allowed simultaneous imaging of the tumor microvasculature and quantification of oxygen partial pressures. From lifetime images using the red-emitting intracellular oxygen probe BTPDM1 and the green-emitting intravascular fluorescent probe FITC-dextran, we demonstrated hypoxic heterogeneity in the TME with a sparse vascular network and showed that the oxygen levels of tumor cells gradually decreased with vascular distance.

The vascular structures within tumors differ significantly from those of normal tissues due to dysregulated angiogenesis^{1–3}. The impaired vascular network in tumors causes an imbalance between oxygen (O_2) supply and consumption in tissues, resulting in inhomogeneous O_2 distribution, including localized hypoxia. Hypoxic (O_2 deficient) conditions are a prevalent feature of various solid tumors that alters the expression of genes that regulate metabolism and other processes, and this is closely related to cancer cell proliferation, migration, and invasion^{4,5}. Furthermore, tumor hypoxia is associated with resistance to radiotherapy, chemotherapy, and phototherapy, making elucidation of the hypoxic microenvironment, including the tumor vasculature, of great importance for clinical applications.

A variety of methods have been developed to image the vascular structures of tissues, including computed tomography (CT)^{6,7}, magnetic resonance imaging (MRI)⁸, photoacoustic imaging⁹, and optical imaging^{10–12}. These techniques enable visualization of the disorganized vasculature of tumors. CT and MRI have also been applied clinically to track radiotherapy-associated changes in vascular structure. By comparison, methods for imaging tissue oxygenation have also been developed and include polarographic assays, EPR oximetry, MRI, CT, positron emission tomography (PET), nuclear magnetic resonance (NMR) relaxation^{13–15}, and optical imaging using phosphorescent probes¹⁶. Among these techniques, phosphorescent probe methods have a great advantage of allowing simultaneous imaging of vascular structures and O_2 levels at the cellular level, although they have a low tissue penetration depth (≤ 1 mm).

The development of superior luminescent probes represented the key advancement in phosphorescent probe technology^{17–19}. The major requirements for intravascular probes are as follows: the probe remains in the blood

¹Division of Molecular Science, Graduate School of Science and Technology, Gunma University, 1-5-1 Tenjin-Cho, Kiryu, Gunma 376-8515, Japan. ²Molecular Pharmacology and Oncology, Graduate School of Medicine, Gunma University, 3-39-22, Showa-machi, Maebashi, Gunma 371-8511, Japan. ✉email: yoshihara@gunma-u.ac.jp

for a sufficient time without being taken up into cells; it is stable in blood and exhibits sufficiently low biological toxicity; and the luminescence lifetime is sensitive to blood O_2 concentration, allowing detection of subtle differences in blood O_2 partial pressure (pO_2). Vinogradov and coworkers developed a water-soluble dendritic probe with a porphyrin metal complex core and used it to successfully image microvascular and interstitial O_2 in the brain, bone marrow, and retinal tissue *in vivo* using a phosphorescence lifetime imaging microscopy (PLIM) approach^{20–23}. Another study reported that compared with conventional phosphorescence imaging, pO_2 images of much deeper layers of tumors can be acquired simultaneously with radiation therapy using radiotherapy-induced Cherenkov light to excite dendritic probes administered to mice²⁴. Metalloporphyrin probes are excitable and emit light in the red and near-infrared region (600–900 nm), and they exhibit high O_2 sensitivity due to long phosphorescence lifetimes²⁵. Another type of metal complex-based O_2 probe, the Ir(III) complex, is reportedly useful for O_2 imaging in cultured cells and biological tissues^{26–31}. Ligand modification of Ir(III) complexes is relatively easy and encompasses a diverse range of possibilities, which is advantageous for developing O_2 probes suitable for varied applications.

In previous studies, we performed high-resolution imaging of the O_2 distribution in kidney, liver, and pancreatic tissues using Ir(III) complexes that are moderately lipophilic, taken up into cells efficiently, and emit strong phosphorescence^{32–35}. Furthermore, we showed that Ir(III) complexes can also be used as a blood O_2 probe by introducing hydrophilic polyethylene glycol (PEG) chains into the ligand of BTP ((*btp*)₂Ir(acac) (*btp* = benzo-thienylpyridine, acac = acetylacetone)) (Fig. 1)^{35,36}. In these previous studies, we used the primary amine of PEG_n ($n = 48$, where n is the number of ethylene glycol units; MW = 2145.58) to generate lipophilic Ir(III) complex BTP that is also water soluble. However, disadvantages of this synthesized Ir(III) complex included low blood retention and slow uptake into cells. Therefore, in the present study, we synthesized a PEGylated Ir(III) complex, BTP-PEGm (where $m = 2000, 5000, 10000, 20000$ and denotes the average molecular weight of one PEG chain) (Fig. 1), which has PEG chains with different lengths in the ligands. We then compared the effects of the differing-length PEG chains on blood retention and cell membrane permeability. Using the most suitable BTP-PEGm as a blood O_2 probe, we investigated the effect of vascular structure on blood pO_2 distribution in tumor tissues. We also investigated the relationship between vascular structure and intracellular pO_2 distribution using the intracellular O_2 probe BTPDM1 and vascular staining reagent FITC-dextran (500 kDa).

Results and discussion

Photophysical properties of BTP-PEGm in solution and medium of cultured cells

We first investigated the photophysical properties of BTP-PEGm in saline. All of the PEGylated derivatives of BTP showed high solubility in aqueous media and exhibited similar absorption and phosphorescence spectra in saline (Fig. S1). They also exhibited relatively large molar absorption coefficients of $(8.6–9.2) \times 10^3 \text{ dm}^3 \text{ mol}^{-1} \text{ cm}^{-1}$ at 488 nm and phosphorescence spectra with a maximum at 644 nm and sufficiently high quantum yield of ~ 0.17 under degassed conditions (Table 1). The phosphorescence decay profiles followed a single exponential decay pattern with phosphorescence lifetimes varying from $\sim 4.0 \mu\text{s}$ to $\sim 0.9 \mu\text{s}$ in degassed and aerated saline (Fig. S2, Table 1). These results demonstrate that BTP-PEGm exhibits excellent photophysical properties as an O_2 probe in aqueous medium.

As intravascular O_2 probes must not interact with proteins such as albumin or be taken up by cells when administered into the blood, we next investigated the photophysical properties of BTP-PEGm in fetal bovine serum (FBS). The phosphorescence spectra of BTP-PEGm in FBS (Fig. S3) were almost identical to those in saline, except that in FBS, autofluorescence was superimposed around 500–600 nm when excited at 488 nm. The phosphorescence decays could be fitted with a single-exponential function, although the residuals were slightly

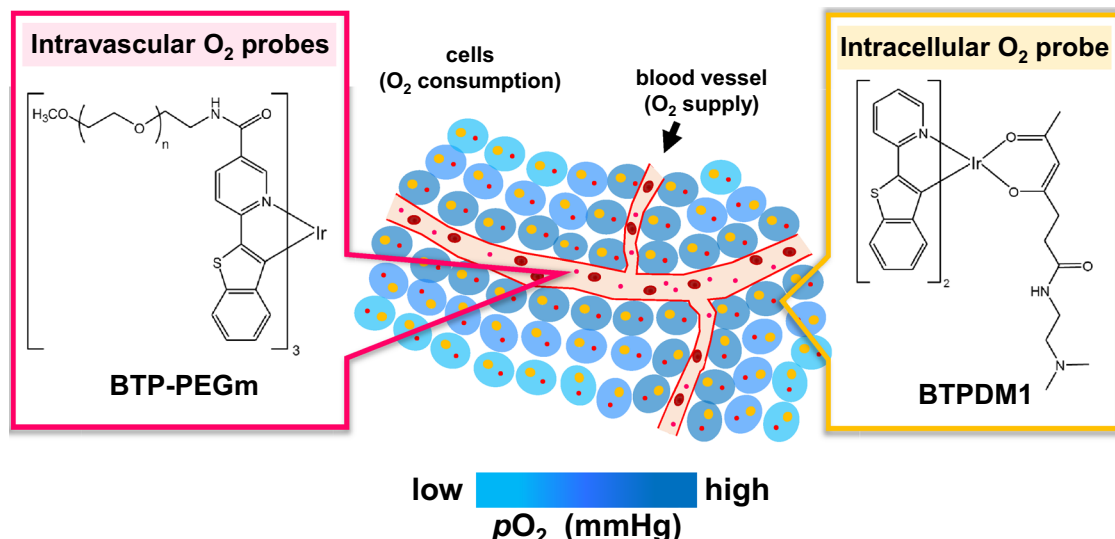


Figure 1. Chemical structures of intravascular and intracellular O_2 imaging probes based on Ir(III) complexes.

Compound	Average molecular weight	ϵ^a (10^3 $\text{dm}^3 \text{ mol}^{-1} \text{ cm}^{-1}$)	$\lambda_{\text{max}}^{\text{Phos}}(\text{nm})$	$\tau_p^0(\mu\text{s})$	$\tau_p(\mu\text{s})$	Φ_p^0 ^b	Φ_p ^b
BTP-PEG2000	7300	9.2	644	3.89	0.89	0.16	0.05
BTP-PEG5000	16,000	9.0	644	4.01	0.90	0.17	0.05
BTP-PEG10000	32,000	8.7	644	4.04	0.87	0.17	0.05
BTP-PEG20000	63,000	8.6	644	4.04	0.93	0.17	0.05

Table 1. Photophysical properties of BTP-PEGm in saline at 37 °C. ^aAt 488 nm. ^bAt room temperature.

distorted for BTP-PEG2000 (Fig. S4), probably due to the effect of albumin present in the FBS. These results revealed that interaction between the phosphorescent group BTP and albumin molecules was sufficiently suppressed in BTP-PEGm complexes other than BTP-PEG2000.

The cell permeability of BTP-PEGm was examined by adding the complex to medium of cultured HCT-116 cells and then determining the emission intensity and acquiring PLIM images. The results for BTP-PEG10000 are shown in Fig. 2. Autofluorescence images for each cell (Fig. 2a, left) revealed the position of that cell in the medium. The phosphorescence intensity images showed that the luminescence of BTP-PEG10000 was almost exclusively limited to the culture medium, indicating that very little probe had entered the cells. PLIM images taken under culture conditions of 21% and 2.5% O₂ and distribution histograms of probe lifetime demonstrated that the phosphorescence lifetime of BTP-PEG10000 depends significantly on the concentration of O₂ in the medium. The other derivatives, BTP-PEG5000 and BTP-PEG20000, gave results similar to BTP-PEG10000, whereas BTP-PEG2000 also exhibited emission from inside the cells (Figs. S5–S7). These data indicate that some proportion of BTP-PEG2000 passes through the cell membrane and remains within the cell.

Characterization of BTP-PEGm as an intravascular O₂ probe

The results of experiments using cultured cells revealed that the various BTP-PEGm probes, other than BTP-PEG2000, were not taken up into cells but rather remained in the medium and exhibited oxygen-sensitive phosphorescence. Application of BTP-PEGm as an intravascular oxygen probe requires that the complex remains in the bloodstream long enough and retains its photophysical properties. Therefore, we investigated the behavior of BTP-PEGm in renal tissues by injecting the probe into the tail vein of an anesthetized mouse. A schematic illustration of the renal surface is depicted in Fig. S8, together with an illustration of the typical renal surface of a mouse administered BTPDM1 and FITC-lectin, as reported in our previous paper³². In the kidney, the glomeruli first filter waste products from the blood and produce primary urine, and then the necessary components in the primary urine are reabsorbed in the proximal tubules (Fig. S8a). Areas of intense fluorescence (Fig. S8b), due primarily to FITC-lectin, indicate the locations of peritubular capillaries, and areas of intense phosphorescence (Fig. S8c) indicate BTPDM1 taken up by tubular cells. These images provide a clear visualization of the micro-architecture of the renal surface tissue, including tubular cells, peritubular capillaries, and the urinary space.

Figure 3 shows images of phosphorescence intensity in renal tissues (ca. 10 μm from the surface) of mice administered 100 nmol of BTP-PEGm (100 μL saline solution). By comparing the images in Fig. 3a with those of Fig. S8, we find that the retention of BTP-PEGm in the bloodstream varies greatly depending on the length of the PEG chains. Images of phosphorescence intensity taken 10 min and 30 min after administration showed the presence of BTP-PEG2000 not only in peritubular capillaries but also in tubular cells and the urinary space. This indicates that intravenously administered BTP-PEG2000 is filtered by the glomeruli within approximately 10 min and transferred from the blood to the primary urine. A similar trend was observed with BTP-PEG5000, although the migration rate was much slower than that of BTP-PEG2000. By contrast, Fig. 3b demonstrates that BTP-PEG10000 and BTP-PEG20000 are retained in the blood without being filtered by the glomeruli, even 4 h after administration. A possible reason why BTP-PEG10000 and BTP-PEG20000 are not filtered in the glomerulus lies in their high molecular weight (MW) and molecular size. The threshold MW for glomerular filtration is estimated at approximately 30–50 kDa, depending on molecule shape, molecular structure, and flexibility^{37,38}. For example, albumin and hemoglobin, which both have a molecular weight of ~ 67 kDa, are not filtered by the glomerulus. The reason why BTP-PEG20000 does not pass through the glomerular capillary wall can be explained by its average molecular weight (~ 63 kDa), similar to that of albumin and hemoglobin. Although the MW of BTP-PEG10000 (~ 32 kDa) is near the threshold for filtration, the glomerular barrier is also known to be highly size selective³⁹. Dynamic light scattering measurements indicated that the hydrodynamic radius of albumin is 3.37 nm⁴⁰. As the calculated Stokes radius of one PEG10000 unit is ~ 2.9 nm⁴¹, the estimated radius of the entire BTP-PEG10000 molecule would be greater than that of albumin and also that (~ 4 nm) of the glomerular pores³⁷. We also acquired phosphorescence intensity images of the surface of hepatic tissue of mice administered 100 nmol of BTP-PEG10000 or BTP-PEG20000 (100 μL saline solution). As shown in Fig. S9, the sinusoid network could be clearly visualized 30 min and 4 h after administration, indicating that neither BTP-PEG10000 nor BTP-PEG20000 was taken up by hepatic cells.

These results indicate that BTP-PEG10000 and BTP-PEG20000 exhibit excellent properties as intravascular O₂ probes. However, considering the ease of administration to mice, BTP-PEG10000 is preferable because it has a lower molecular weight and lower viscosity when dissolved in saline. Therefore, we used BTP-PEG10000 as an O₂ probe in subsequent experiments.

Before proceeding to quantitative measurements, however, we investigated the photostability and the O₂ response of BTP-PEG10000 in peritubular capillaries. The photostability of BTP-PEG10000 in peritubular capillaries was evaluated by acquiring 10 PLIM images of the surface of the kidney in the same field of view. The

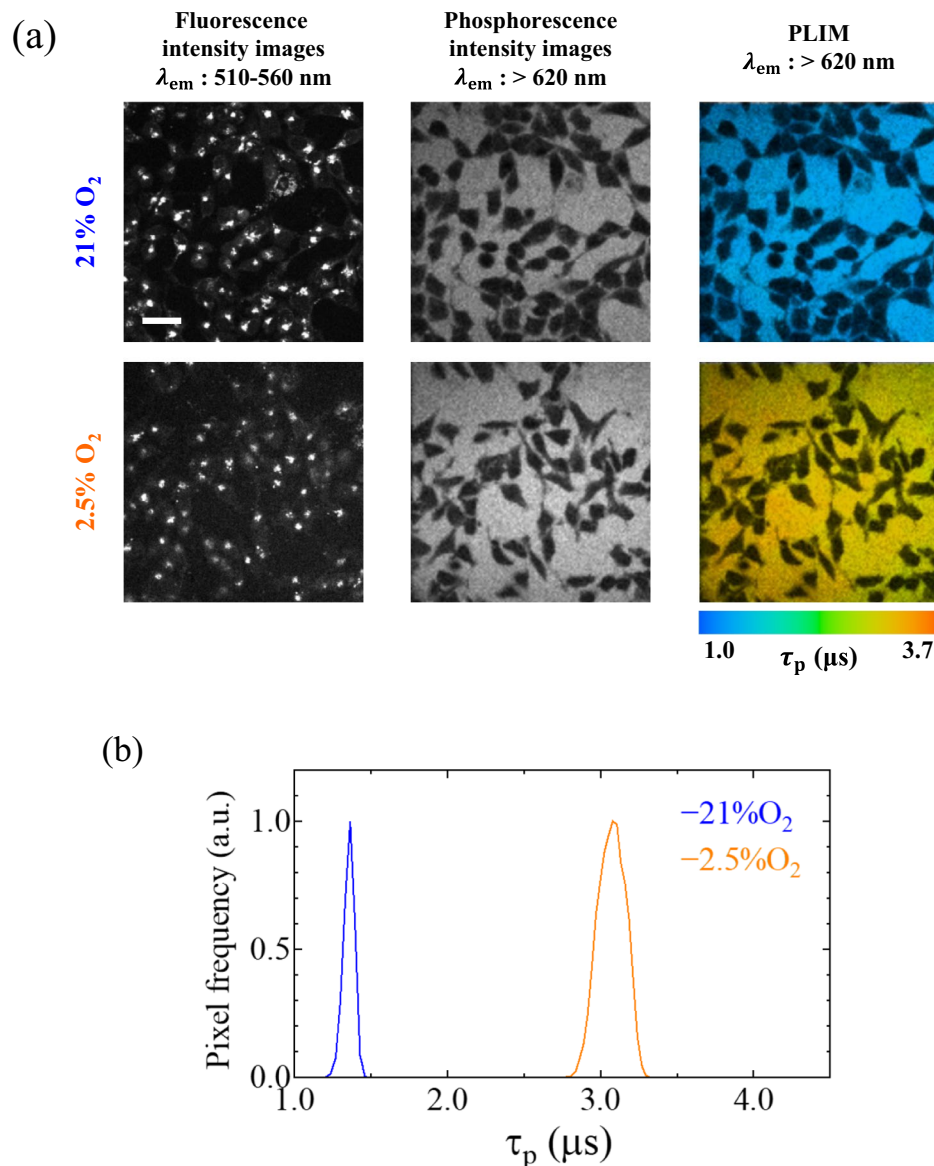


Figure 2. (a) Fluorescence and phosphorescence intensity images and PLIM images of HCT-116 cells incubated in culture medium containing BTP-PEG10000 (10 μM) for 30 min at 37 $^{\circ}\text{C}$ under 21% and 2.5% O₂ conditions. Excitation wavelength: 488 nm; collected emission wavelength range for fluorescence intensity images: 510–560 nm; and collected emission wavelength range for phosphorescence intensity and PLIM images: > 620 nm. Scale bar: 50 μm . (b) Distribution histograms of phosphorescence lifetimes for the PLIM images shown in (a).

decrease in relative emission intensity was < 5% (Fig. S10), indicating that BTP-PEG10000 has sufficient photostability for successive PLIM measurements of the same field of view. We then examined the O₂ response of BTP-PEG10000 in peritubular capillaries by changing the inspired O₂ concentration of mice, which was adjusted using O₂/N₂ mixed gas. First, we acquired PLIM images of kidney tissue at a normal O₂ concentration (21%), and after 2.5 min, the O₂ concentration was reduced to 15% and PLIM images acquired. After 7.5 min, the O₂ concentration was changed back to 21%, and PLIM images were again acquired. Figure 4a,b show the PLIM images of renal tissues and the average probe lifetimes, respectively, along with the time of measurement. Histograms showing probe lifetime for each image are shown in Fig. 4c. These data demonstrate that the phosphorescence lifetime of BTP-PEG10000 reversibly reflects the subtle changes in O₂ concentration that occur in peritubular capillaries.

The biocompatibility of BTP-PEG10000 is an important factor for potential in vivo application. To examine biocompatibility, saline (100 μL) or a stock saline solution of BTP-PEG10000 (100 μL) was injected into the tail vein of mice. No probe-induced abnormal behavior or weight loss was observed during the observation period (7 days) in any of the mice (Fig. S11), suggesting that BTP-PEG10000 is not acutely toxic in mice.

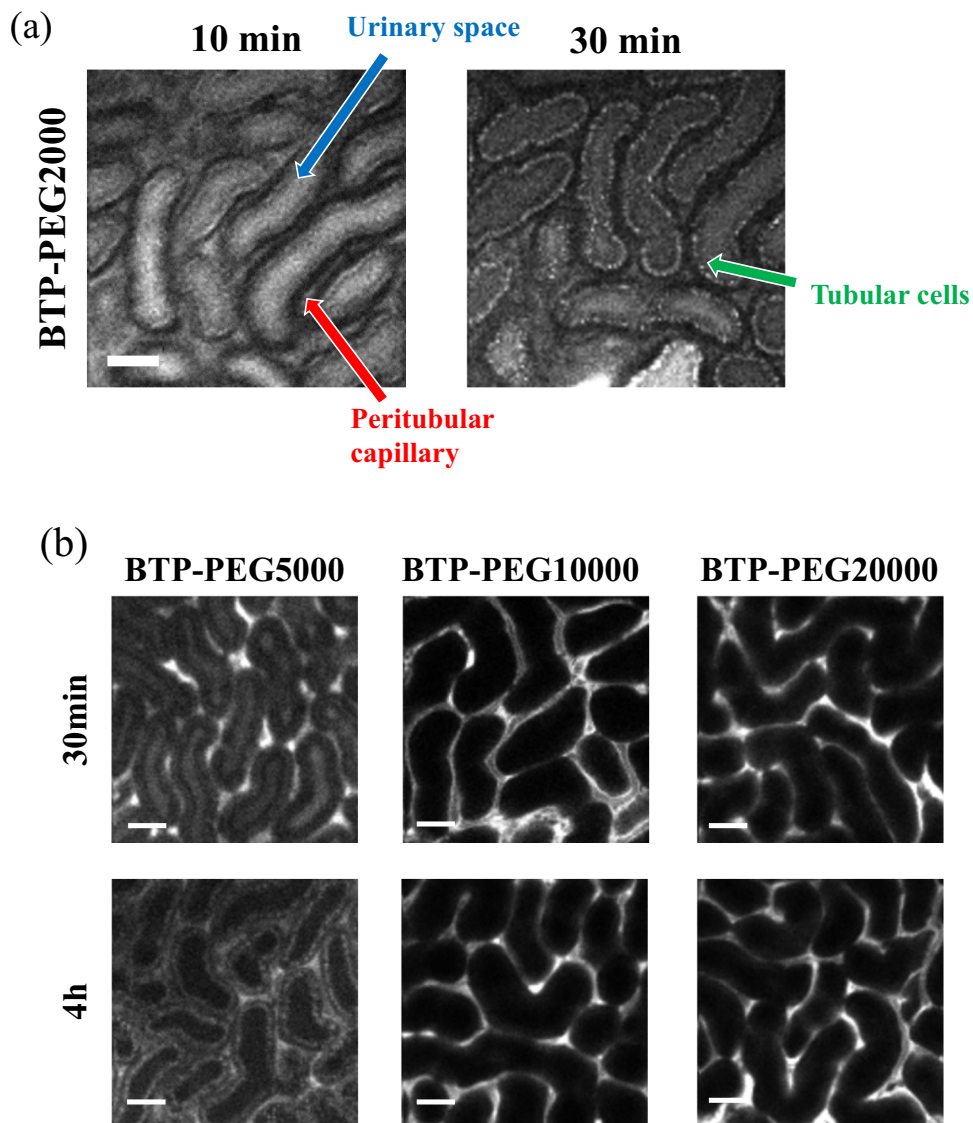


Figure 3. (a) Emission intensity images of the surface of the kidney of a mouse at 10 and 30 min after administration of BTP-PEG2000 (100 nmol). (b) Emission intensity images of the surface of the kidneys of mice at 30 min and 4 h after administration of BTP-PEG5000, 10000, or 20000 (100 nmol). Excitation wavelength: 488 nm; collected emission wavelength range: > 620 nm. Scale bars: 50 μ m.

Intravascular O_2 imaging in tumor tissues using BTP-PEG10000

As it was confirmed that the phosphorescence lifetime of BTP-PEG10000 is sensitive to changes in the O_2 concentration in the renal capillaries, we quantitatively investigated the relationship between the phosphorescence lifetime of BTP-PEG10000 and pO_2 using mouse plasma. The lifetime (τ_p^0) of BTP-PEG10000 in deoxygenated plasma was almost constant at three different temperatures close to the body temperature of mice under anesthesia (Table S1). Stern–Volmer plots of τ_p^0/τ_p versus pO_2 for BTP-PEG10000 in blood plasma exhibited straight lines with differing slopes at these temperatures (Fig. S12a). The quenching rate constant (k_q) derived from the plot shown in Fig. S12a increased at higher temperatures (Fig. S12b), because the molecular diffusion rate increases with increasing temperature. The pO_2 at each pixel in a PLIM image can be determined using the lifetime (τ_p) of BTP-PEG10000 according to the equation $pO_2 = (1/k_q)(1/\tau_p - 1/\tau_p^0)$, as derived from the Stern–Volmer equation. In the experiments discussed below, we used the average τ_p^0 at three temperatures and the k_q value at the body temperature of the mouse during the PLIM measurements.

First, we administered BTP-PEG10000 (100 nmol in saline) to tumor-bearing mice under anesthesia, removed a section of skin to expose the tumor, and then acquired PLIM images of the tumor tissue. A typical PLIM image and a partially magnified image of tumor tissue measured using 4 \times and 10 \times objectives are shown in Fig. 5 along with corresponding intensity images. The phosphorescence of BTP-PEG10000 enabled clear visualization of the tumor microvasculature, with its characteristic chaotic and tortuous morphology. Such heterogeneity in tumor vascular architecture is thought to be closely associated with hypoxia in solid tumors^{42,43}. However, few

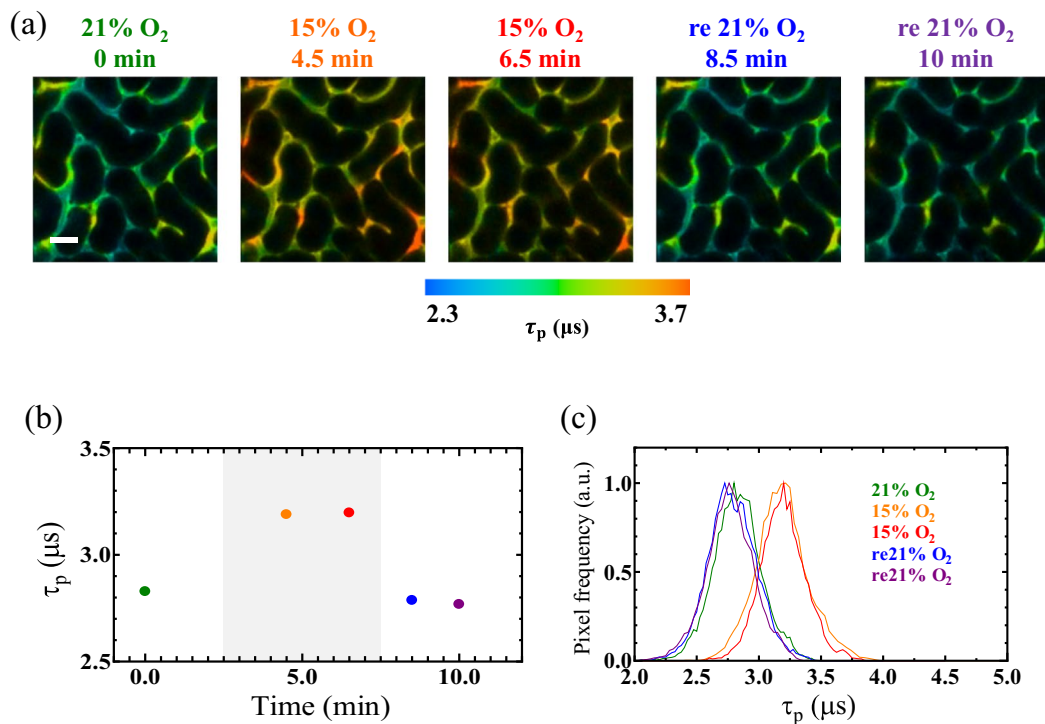


Figure 4. (a) PLIM images of the surface of the kidney of a mouse under different inspired $p\text{O}_2$ conditions: 0–2.5 min (21% O_2), 2.5–7.5 min (15% O_2), >7.5 min (return to 21% O_2). BTP-PEG10000 was administered prior to the PLIM measurements. Excitation wavelength: 488 nm; collected emission wavelength range: >620 nm. Scale bar: 50 μm . (b) Changes in average phosphorescence lifetimes for the PLIM images shown in (a). (c) Distribution histograms of phosphorescence lifetimes for the PLIM images shown in (a).

studies have simultaneously visualized in detail the tumor vasculature and O_2 distribution *in vivo*. Therefore, we calculated the $p\text{O}_2$ distribution of tumor vessels from PLIM images. The decay curves calculated for different locations in Fig. 5 followed single-exponential functions and indicated markedly different lifetimes (Fig. S13), thus revealing the heterogeneity of oxygen status within the tumor tissue (Table S2). Figure 5b,c show the lifetime distribution in PLIM images acquired with 4 \times and 10 \times objectives and the $p\text{O}_2$ distributions calculated from the lifetimes, respectively. Figure 5 shows that the blood vessels near the center of the image have a narrow and intricate structure and that the O_2 concentrations are much lower compared with the surrounding thicker blood vessels. We acquired similar PLIM measurements at different locations in the tumor (Fig. S14). These images showed that the oxygen level varied depending on the hypoxic heterogeneity in the tumor microenvironment (TME) with a sparse vascular network. In contrast, the $p\text{O}_2$ distribution of normal tissue (e.g., kidney) was narrower than that of tumors due to the nearly uniform thickness of the capillaries in normal tissue (Fig. S15).

Intracellular O_2 imaging in tumor tissues using BTPDM1

Using hydrophobic BTPDM1 as an intracellular O_2 probe, we previously reported that the O_2 levels in tumor tissue are considerably lower than those in normal tissue⁴³. Using the same probe, BTPDM1, we also performed high-resolution imaging of tissue oxygenation in the kidney³² and liver³³ of living mice. In the previous section, we found that intravascular O_2 levels in tumor tissue are inhomogeneous, probably due to the irregular vascular structure of tumor tissues. We therefore investigated the relationship between vasculature and intracellular O_2 levels within tumor tissue using BTPDM1 as an O_2 probe. As BTPDM1 emits red phosphorescence with a similar spectrum as BTP-PEG10000, we used FITC-dextran (500 kDa), which emits green fluorescence, for vascular imaging. The absorption and phosphorescence spectra and phosphorescence decay of BTPDM1 in aerated and de-aerated acetonitrile are shown in Fig. S16. The phosphorescence spectrum of BTPDM1 in acetonitrile exhibited a vibrational pattern, but the wavelength range was almost the same as that of BTP-PEG10000. The lifetime of BTPDM1 internalized in HCT-116 cells at 37 °C varied with the $p\text{O}_2$ in the incubator, as shown in Fig. S17a, and the quenching rate constant was determined for three different temperatures from Stern–Volmer plots (Fig. S17, Table S3).

As we were able to determine the relationship between the lifetime of BTPDM1 in HCT-116 cells and the $p\text{O}_2$ in the incubator, we next performed PLIM/FLIM analyses of tumor tissues using BTPDM1 as an intracellular probe and FITC-dextran as a vasculature imaging reagent. FITC-dextran (100 μg , 100 μL in saline) was administered to a tumor-bearing mouse approximately 1 h after administration of BTPDM1 (250 nmol, 150 μL in saline containing 10% DMSO), followed by PLIM measurements. A typical PLIM image of a tumor in the mouse administered BTPDM1 is shown in Fig. 6, along with an image of FITC-dextran fluorescence intensity,

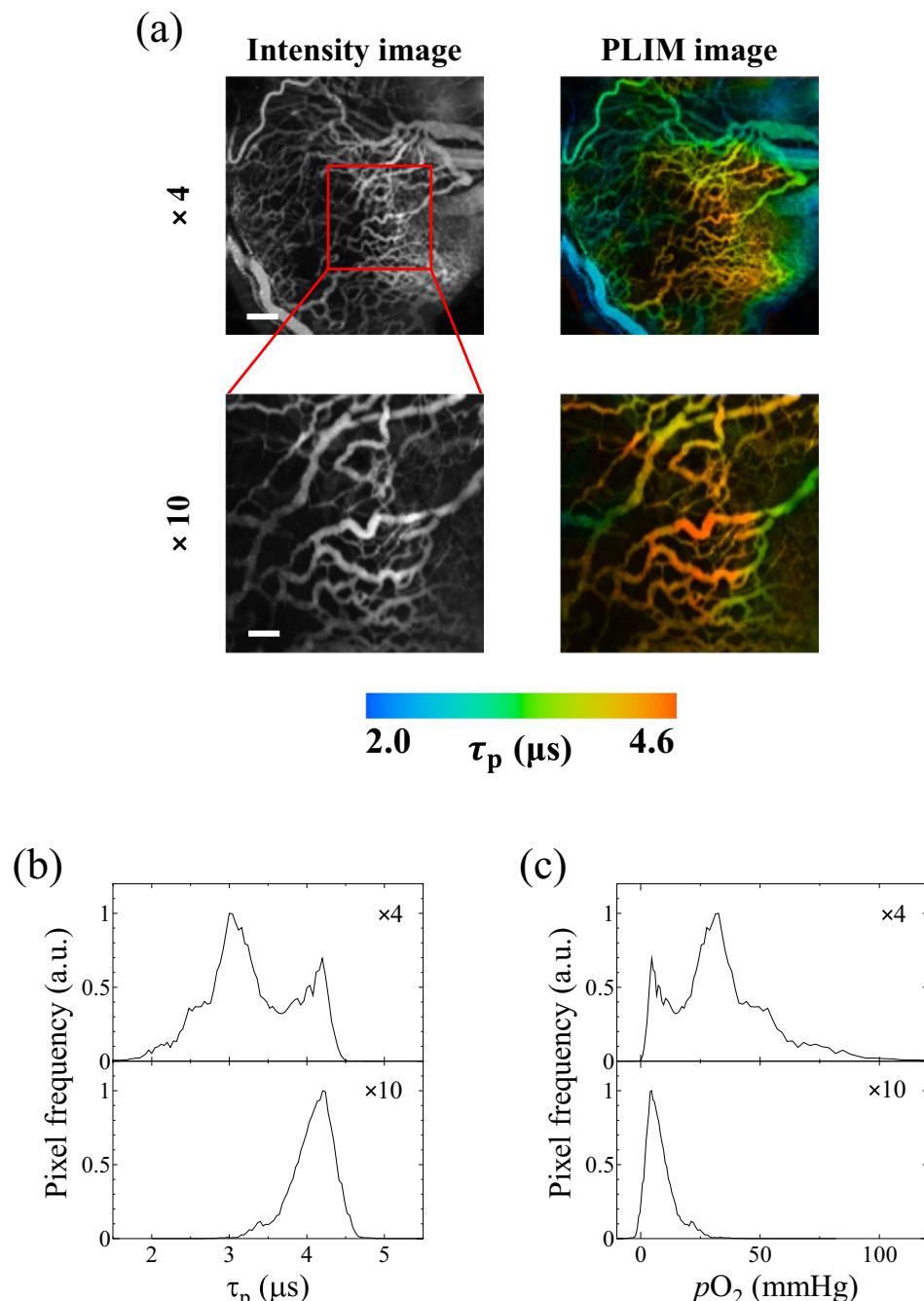


Figure 5. (a) Emission intensity and PLIM images of tumor tissue of a mouse administered BTP-PEG10000 (100 nmol). Upper images: 4× objective lens. Lower images: 10× objective lens. Excitation wavelength: 488 nm; collected emission wavelength range: > 620 nm. Scale bar: 500 μ m (upper images), 200 μ m (lower images). (b,c) Distribution histograms of phosphorescence lifetimes and pO_2 values for PLIM images shown in (a).

which reveals the vasculature (Fig. S18). It can be seen from these images that a pO_2 gradient exists, such that the intracellular O_2 levels decrease as distance from relatively large blood vessels increases. Examining the distance dependence of intracellular O_2 levels from the nearest blood vessel within the region of interest indicated in Fig. 6b, we found that the pO_2 decreased from approximately 30 mmHg to < 10 mmHg over a distance of approximately 150 μ m. This agrees well with the generally expected pO_2 gradient with distance from blood vessels^{13,44}.

Figure 7 shows FLIM/PLIM images taken using a low-magnification objective to observe the intracellular pO_2 distribution over a broader area. The FLIM image depicts a non-uniformly distributed and tortuous vascular network, similar to that shown in Fig. 5. Furthermore, it can be noted from the PLIM image and lifetime distribution that the pO_2 distribution is heterogeneous (i.e., some regions exhibit anomalously low pO_2). Comparing the FLIM and PLIM images reveals that tumor cells in areas with less-developed vascular networks undergo

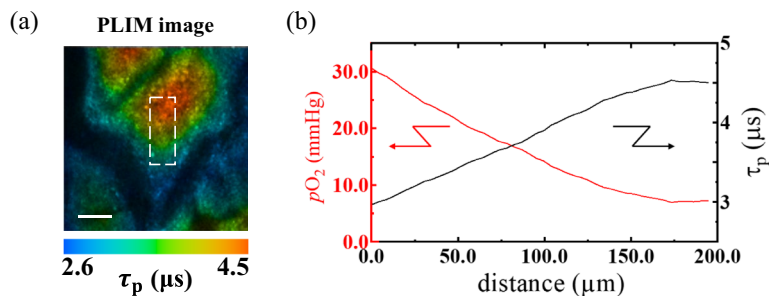


Figure 6. (a) PLIM image of tumor tissue of a mouse administered BTPDM1 (250 nmol). Excitation wavelength: 488 nm; collected emission wavelength range: > 590 nm. Scale bar: 100 μ m. (b) Average phosphorescence lifetimes (black solid line) and average pO_2 values (red solid line) along the white dotted area in the PLIM image.

hypoxia. This hypoxic microenvironment is closely associated with cancer cell proliferation, therapy resistance, and the tumor immune response^{45,46}. In the future, it may be possible to use this method to track the dynamic oxygenation status of chronic and acute hypoxia, which can fluctuate over a period of several minutes.

Conclusions

To develop an optical probe that enables simultaneous imaging of the microvasculature in xenograft tumors in mice and the blood O_2 concentration over a long retention time, we designed and synthesized BTP-PEGm (where $m = 2000, 5000, 10000$, or 20000), PEGylated derivatives of Ir(III) complex BTP. All BTP-PEGm probes showed excellent photophysical properties as an O_2 probe in aqueous medium. The basic performance as a blood O_2 probe *in vivo* was evaluated by acquiring PLIM images of the kidney of mice administered BTP-PEGm. Among the various BTP-PEGm probes examined, BTP-PEG10000 was found to be the most suitable considering its cell permeability, blood retention, and ease of intravenous administration to mice. BTP-PEG10000 exhibited high O_2 sensitivity in blood plasma, with a quenching rate constant of 3.83×10^3 mmHg $^{-1}$ s $^{-1}$ at 37 °C. PLIM images of tumors of mice administered BTP-PEG10000 clearly demonstrated the heterogeneous tumor microvasculature and the wide vasculature-dependent variations in O_2 levels. PLIM images of tumors of mice administered the intracellular O_2 probe BTPDM1 and the intravascular probe FITC-dextran revealed that the tumor cells in areas in which the vascular network was poorly developed exhibited hypoxic heterogeneity, suggesting that the TME is closely linked to cancer cell proliferation, therapy resistance, and the tumor immune response. These results demonstrate that PLIM measurements using BTP-PEG10000 and BTPDM1 as an intravascular O_2 probe and intracellular O_2 probe, respectively, enable high-resolution imaging of tumor microvascular structures, pO_2 in the bloodstream, and intracellular O_2 distributions.

Methods

Materials

BTP-PEGm ($m = 2000, 5000, 10000, 20000$) probes were synthesized and characterized according to the methods described in the Supplementary Information. BTPDM1 was previously synthesized in our laboratory⁴³. Saline (Otsuka) was used as received.

Spectral and photophysical properties in saline

Absorption spectra of BTP-PEGm in saline at room temperature were acquired using a UV/Vis spectrophotometer (Ubest-V550, JASCO). Emission spectra were recorded on a system consisting of a monochromatized 150 W Xe arc lamp, a sample holder, and a photonic multichannel analyzer (PMA-12, C11027-01, Hamamatsu Photonics). Emission spectra were fully corrected for spectral sensitivity. Emission quantum yields were measured using an absolute photoluminescence quantum yield measurement system (C9920-02, Hamamatsu Photonics)⁴⁷. Emission lifetimes were measured using a lifetime measurement system (Quantaurus-Tau, C11367G, Hamamatsu Photonics) based on a time-correlated single-photon counting method. A laser diode (PLP-10, Hamamatsu Photonics; wavelength: 481 nm, pulse width: 70 ps) was used as the excitation light source. The temperature of sample solution was controlled by circulating water from a temperature-controlled bath (RTE7, Neslab) through a jacketed cuvette holder.

FLIM and PLIM imaging system

Confocal fluorescence and phosphorescence intensity and lifetime images were measured using an inverted fluorescence microscope (IX73, Olympus) equipped with a confocal scanning system (DCS-120, Becker & Hickl) and a picosecond diode laser (BDL-SMC, Becker & Hickl; wavelength: 488 nm, pulse width: 40–90 ps, repetition rate: 50 MHz)³³. Emission signals were detected using a hybrid detector module (HPM-100-40, Becker & Hickl). Fluorescence and phosphorescence decay curves were determined using a time-correlated, single-photon counting unit and a multichannel scaler unit (Simple-Tau-150-DX, Becker & Hickl), respectively. Scanning was performed at a frame time of 0.452 s for FLIM and 1.036 s for PLIM. The total acquisition time was 22.6 s for FLIM and 51.8 s for PLIM, corresponding to an accumulation of 50 frames. Emission signals were acquired at

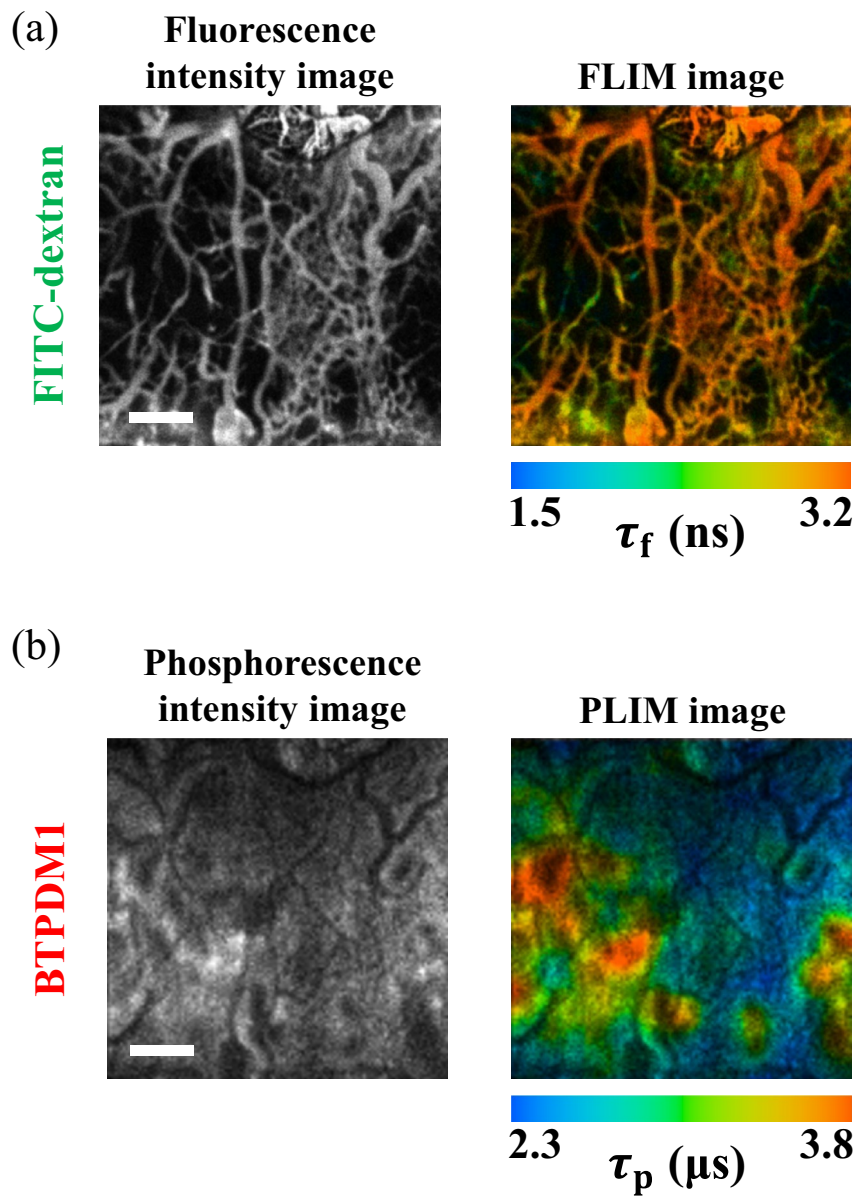


Figure 7. (a) Fluorescence intensity and FLIM images and (b) phosphorescence intensity and PLIM images of tumor tissue of a mouse administered FITC-dextran (average molecular weight: 500 kDa; 1 mg/mL, 100 μ L) and BTPDMI (250 nmol). Excitation wavelength: 488 nm; collected emission wavelength range for fluorescence intensity and FLIM images: 510–560 nm; and collected emission wavelength range for phosphorescence intensity and PLIM images: > 590 nm. Scale bars: 500 μ m.

a spatial resolution of 256×256 pixels for FLIM and 128×128 pixels for PLIM. Fluorescence and phosphorescence lifetime images were generated by analyzing the decay curves for each pixel using SPCImage data analysis software (Becker & Hickl).

Cellular experiments

HCT-116 human colorectal carcinoma cells were purchased from the American Type Culture Collection and cultured in McCoy's 5A medium with 10% FBS (Thermo Fisher Scientific), 1% penicillin (50 units/mL, Thermo Fisher Scientific), and streptomycin (50 μ g/mL, Thermo Fisher Scientific). HCT-116 cells were seeded on glass-bottom dishes (Greiner) and allowed to adhere for 24 h, and then the cells were incubated with BTP-PEGm (10 μ M) for 30 min at 37 °C. Fluorescence and phosphorescence intensity images and PLIM images of HCT-116 cells incubated with BTP-PEGm (10 μ M) under air-saturated and 2.5% O_2 conditions were acquired using an FLIM and PLIM imaging system equipped with a variable temperature and O_2 concentration incubator (INUBTF-WSKMX, GM-8000, Tokai Hit).

Animal handling and ethics

All protocols for animal experiments were approved by the Ethics Committee on Animal Experiments of Gunma University (18-018), and all animal experiments were conducted under the appropriate institutional guidelines. All experiments were performed in compliance with the ARRIVE guidelines. *Balb/c* male mice (7 to 9 weeks old; CLEA Japan) were used in this study. The mice were anesthetized by intraperitoneal injection of a mixed anesthetic (ketamine: 100 mg kg⁻¹, xylazine: 10 mg kg⁻¹ in saline). During imaging experiments, the body temperature of the mice was maintained at 35–37 °C using a body temperature maintenance system (BWT-100A, Bio Research Center) that fed back data regarding the rectal temperature.

Microvascular imaging of kidney tissue

A saline solution of BTP-PEGm (1 mM, 100 µL) was injected into the tail vein of an anesthetized mouse. The kidney was exposed by flank incision, then the mouse was turned with its left kidney on a cover glass chamber (Iwaki). Phosphorescence intensity images were then recorded using a PLIM imaging system. For hypoxemia experiments, the mouse breathed room air or O₂/N₂ mixed gas (15% O₂) prepared using a digital gas mixing system (GM-8000, Tokai Hit).

Subcutaneous transplantation in immunocompromised mice

Tumor transplants were established in 7-week-old athymic nude male mice (Balb/c-nu/nu, CLEA Japan) by subcutaneous injection of a suspension of a total of 5 × 10⁶ HCT-116 cells in 150 µL of diluted Matrigel (Corning)-PBS (1:1 [v/v]). Imaging experiments with tumor-bearing mice were performed 2 or 3 weeks after the injection of tumor cells. The diameter of the tumor was approximately 1 cm.

Intravascular and intracellular O₂ imaging of tumors

For intravascular imaging experiments, a saline solution of BTP-PEG10000 (1 mM, 100 µL) was injected into the tail vein of an anesthetized tumor-bearing mouse. For intracellular imaging experiments, a stock solution of BTPDM1 (1.7 mM) was prepared by dissolving the probe in saline/DMSO (14:1 [v/v]) and injected into the tail vein of an anesthetized tumor-bearing mouse. Approximately 1 h after BTPDM1 administration, a saline solution of FITC-dextran (Sigma, average molecular weight: 500 kDa, 1 mg/mL, 100 µL) was intravenously administered just before imaging experiments. Solid tumors were exposed by peeling of the skin, and then the mouse was turned with the tumor on a cover glass chamber (Iwaki). Phosphorescence intensity and lifetime images were recorded using a PLIM imaging system.

Calculation of pO₂ based on phosphorescence lifetime

Intravascular and intracellular pO₂ values in tumors were determined from phosphorescence lifetime based on calibration curves generated using mouse blood plasma and HCT-116 cultured cells, respectively. Phosphorescence lifetime measurements of BTP-PEG10000 dissolved in mouse blood plasma under different pO₂ at 37 °C were performed using the same PLIM system. Here, under the 0% O₂ condition, Na₂SO₃ (500 mM) was added to the plasma to remove existing O₂. For the calibration of BTPDM1, PLIM images were acquired for HCT-116 cells stained with BTPDM1 (500 nM, 2 h) under different pO₂ values at 37 °C. Except in the case of 0% O₂, the cells were incubated with antimycin A (10 µM, > 0.5 h) to block the effects of cellular respiration. In the 0% O₂ experiments, fresh medium containing Na₂SO₃ (500 mM) was used to remove existing O₂ in the medium. The average phosphorescence lifetimes determined from PLIM images taken under different pO₂ conditions were plotted according to the Stern–Volmer relationship, $\tau_p^0/\tau_p = 1 + k_q \tau_p^0 pO_2$, to determine the bimolecular quenching rate constant (k_q). Intravascular and intracellular pO₂ values in tumors were calculated from the phosphorescence lifetime (τ_p) data using the k_q and τ_p^0 values.

Data availability

The datasets generated during and/or analysed during the current study are available from the corresponding author on reasonable request.

Received: 8 June 2024; Accepted: 5 August 2024

Published online: 08 August 2024

References

1. Siemann, D. W. The unique characteristics of tumor vasculature and preclinical evidence for its selective disruption by tumor-vascular disrupting agents. *Cancer Treat. Rev.* **37**, 63–74 (2011).
2. Bochner, F. *et al.* Intravital imaging of vascular anomalies and extracellular matrix remodeling in orthotopic pancreatic tumors. *Int. J. Cancer* **146**, 2209–2217 (2020).
3. Chen, Z., Han, F., Du, Y., Shi, H. & Zhou, W. Hypoxic microenvironment in cancer: Molecular mechanisms and therapeutic interventions. *Signal Transduct. Target. Ther.* **8**, 70 (2023).
4. Vaupel, P. & Mayer, A. Hypoxia in cancer: Significance and impact on clinical outcome. *Cancer Metastasis Rev.* **26**, 225–239 (2007).
5. Khouzam, R. A. *et al.* Tumor hypoxia regulates immune escape/invasion: Influence on angiogenesis and potential impact of hypoxic biomarkers on cancer therapies. *Front. Immunol.* **11**, 613114 (2021).
6. Zopf, L. M. *et al.* Cross-modality imaging of murine tumor vasculature: A feasibility study. *Mol. Imaging Biol.* **23**, 874–893 (2021).
7. Alilou, M. *et al.* A tumor vasculature-based imaging biomarker for predicting response and survival in patients with lung cancer treated with checkpoint inhibitors. *Sci. Adv.* **8**, 4609 (2022).
8. Pathak, A. P., Penet, M.-F. & Bhujwalla, Z. M. MR molecular imaging of tumor vasculature and vascular targets. *Adv. Genet.* **69**, 1–30 (2010).
9. Toi, M. *et al.* Visualization of tumor-related blood vessels in human breast by photoacoustic imaging system with a hemispherical detector array. *Sci. Rep.* **7**, 41970 (2017).

10. Yamauchi, F., Kamioka, Y., Yano, T. & Matsuda, M. *In vivo* FRET imaging of tumor endothelial cells highlights a role of low PKA activity in vascular hyperpermeability. *Cancer Res.* **76**, 5266–5276 (2016).
11. Demidov, V. *et al.* Preclinical longitudinal imaging of tumor microvascular radiobiological response with functional optical coherence tomography. *Sci. Rep.* **8**, 38 (2018).
12. Karrobi, K., Tank, A., Tabassum, S., Pera, V. & Roblyer, D. Diffuse and nonlinear imaging of multiscale vascular parameters for *in vivo* monitoring of preclinical mammary tumors. *J. Biophotonics* **12**, e201800379 (2019).
13. Vaupel, P., Flood, A. B. & Swartz, H. M. Oxygenation status of malignant tumors vs. normal tissues: Critical evaluation and updated data source based on direct measurements with pO_2 microsensors. *Appl. Magn. Reson.* **52**, 1451–1479 (2021).
14. Swartz, H. M. *et al.* How best to interpret measures of levels of oxygen in tissues to make them effective clinical tools for care of patients with cancer and other oxygen-dependent pathologies. *Physiol. Rep.* **8**, e14541 (2020).
15. Mittal, S. & Mallia, M. B. Molecular imaging of tumor hypoxia: Evolution of nitroimidazole radiopharmaceuticals and insights for future development. *Bioorg. Chem.* **139**, 106687 (2023).
16. Wilson, D. F. & Cerniglia, G. L. Localization of tumors and evaluation of their state of oxygenation by phosphorescence imaging. *Cancer Res.* **52**, 3988–3993 (1992).
17. Liu, J. N., Bu, W. & Shi, J. Chemical design and synthesis of functionalized probes for imaging and treating tumor hypoxia. *Chem. Rev.* **117**, 6160–6224 (2017).
18. Zheng, X. *et al.* A near-infrared phosphorescent nanoprobe enables quantitative, longitudinal imaging of tumor hypoxia dynamics during radiotherapy. *Cancer Res.* **79**, 4787–4797 (2019).
19. Zhdanov, A. V. *et al.* Analysis of tumour oxygenation in model animals on a phosphorescence lifetime based macro-imager. *Sci. Rep.* **13**, 18732 (2023).
20. Esipova, T. V. *et al.* Oxyphor 2P: A high-performance probe for deep-tissue longitudinal oxygen imaging. *Cell Metab.* **29**, 736–744. e7 (2019).
21. Spencer, J. A. *et al.* Direct measurement of local oxygen concentration in the bone marrow of live animals. *Nature* **508**, 269–273 (2014).
22. Christodoulou, C. *et al.* Live-animal imaging of native haematopoietic stem and progenitor cells. *Nature* **578**, 278–283 (2020).
23. Şençan, I. *et al.* Two-photon phosphorescence lifetime microscopy of retinal capillary plexus oxygenation in mice. *J. Biomed. Opt.* **23**, 126501 (2018).
24. Cao, X. *et al.* Tissue pO_2 distributions in xenograft tumors dynamically imaged by Cherenkov-excited phosphorescence during fractionated radiation therapy. *Nat. Commun.* **11**, 573 (2020).
25. Papkovsky, D. B. & Dmitriev, R. Biological detection by optical oxygen sensing. *Chem. Soc. Rev.* **42**, 8700–8732 (2013).
26. Tobita, S. & Yoshihara, T. Intracellular and *in vivo* oxygen sensing using phosphorescent iridium(III) complexes. *Curr. Opin. Chem. Biol.* **33**, 39–45 (2016).
27. Yoshihara, T., Hirakawa, Y., Hosaka, M., Nangaku, M. & Tobita, S. Oxygen imaging of living cells and tissues using luminescent molecular probes. *J. Photochem. Photobiol. C* **30**, 71–95 (2017).
28. Zhang, K. Y. *et al.* Dual-phosphorescent iridium(III) complexes extending oxygen sensing from hypoxia to hyperoxia. *J. Am. Chem. Soc.* **140**, 7827–7834 (2018).
29. Shaikh, S., Wang, Y., Rehman, F. U., Jiang, H. & Wang, X. Phosphorescent Ir(III) complexes as cellular staining agents for biomedical molecular imaging. *Coord. Chem. Rev.* **416**, 213344 (2020).
30. Zhou, J., Li, J., Zhang, K. Y., Liu, S. & Zhao, Q. Phosphorescent iridium(III) complexes as lifetime-based biological sensors for photoluminescence lifetime imaging microscopy. *Coord. Chem. Rev.* **453**, 214334 (2022).
31. Samandarsangari, M. *et al.* Biocompatible phosphorescent O_2 sensors based on Ir(III) complexes for *in vivo* hypoxia imaging. *Biosensors* **13**, 680 (2023).
32. Hirakawa, Y. *et al.* Intravital phosphorescence lifetime imaging of the renal cortex accurately measures renal hypoxia. *Kidney. Int.* **93**, 1483–1489 (2018).
33. Mizukami, K. *et al.* *In vivo* O_2 imaging in hepatic tissues by phosphorescence lifetime imaging microscopy using Ir(III) complexes as intracellular probes. *Sci. Rep.* **10**, 21053 (2020).
34. Mizukami, K., Muraoka, T., Shiozaki, S., Tobita, S. & Yoshihara, T. Near-infrared emitting Ir(III) complexes bearing a dipyrromethene ligand for oxygen imaging of deeper tissues *in vivo*. *Anal. Chem.* **94**, 2794–2802 (2022).
35. Yoshihara, T., Matsumura, N., Tamura, T., Shiozaki, S. & Tobita, S. Intracellular and intravascular oxygen sensing of pancreatic tissues based on phosphorescence lifetime imaging microscopy using lipophilic and hydrophilic iridium(III) complexes. *ACS Sens.* **7**, 545–554 (2022).
36. Yoshihara, T., Hirakawa, Y., Nangaku, M. & Tobita, S. Hydrophilic Ir(III) complexes for *in vitro* and *in vivo* oxygen imaging. In *RSC Detection Science: Quenched-Phosphorescence Detection of Molecular Oxygen: Application in Life Sciences* (eds Papkovsky, D. B. & Dmitriev, R. I.) 71–90 (Royal Society of Chemistry, 2018).
37. Fox, M. E., Szoka, F. C. & Fréchet, J. M. J. Soluble polymer carriers for the treatment of cancer: The importance of molecular architecture. *Acc. Chem. Res.* **42**, 1141–1151 (2009).
38. Ruggiero, A. *et al.* Paradoxical glomerular filtration of carbon nanotubes. *Proc. Natl. Acad. Sci. U. S. A.* **107**, 12369–12374 (2010).
39. Haraldsson, B., Nyström, J. & Deen, W. M. Properties of the glomerular barrier and mechanisms of proteinuria. *Physiol. Rev.* **88**, 451–487 (2008).
40. Valstar, A., Almgren, M., Brown, W. & Vasilescu, M. The interaction of bovine serum albumin with surfactants studied by light scattering. *Langmuir* **16**, 922–927 (2000).
41. Singh, S., Khulbe, K. C., Matsuura, T. & Ramamurthy, P. Membrane characterization by solute transport and atomic force microscopy. *J. Membr. Sci.* **142**, 111–127 (1998).
42. Brown, J. M. & Wilson, W. R. Exploiting tumour hypoxia in cancer treatment. *Nat. Rev. Cancer* **4**, 437–447 (2004).
43. Yoshihara, T. *et al.* Intracellular and *in vivo* oxygen sensing using phosphorescent Ir(III) complexes with a modified acetylacetone ligand. *Anal. Chem.* **87**, 2710–2717 (2015).
44. Mirabello, V., Cortezon-Tamarit, F. & Pascu, S. L. Oxygen sensing, hypoxia tracing and *in vivo* imaging with functional metalloprobes for the early detection of non-communicable diseases. *Front. Chem.* **6**, 27 (2018).
45. Takahashi, H. *et al.* AKT3 is a novel regulator of cancer-associated fibroblasts in head and neck squamous cell carcinoma. *Cancers* **13**, 1233 (2021).
46. Li, Y., Zhao, L. & Li, X.-F. Hypoxia and the tumor microenvironment. *Technol. Cancer Res. Treat.* **20**, 1533033821106304 (2021).
47. Suzuki, K. *et al.* Reevaluation of absolute luminescence quantum yields of standard solutions using a spectrometer with an integrating sphere and a back-thinned CCD detector. *Phys. Chem. Chem. Phys.* **11**, 9850–9860 (2009).

Acknowledgements

This work was supported by JSPS KAKENHI (Grant Numbers: 22H03919 to T.Y., 19K07706 to S.R.) and AMED (Grant Numbers: JP22gm1210011 to T.Y., DNW-19016 to S.R.). We thank Prof. Emeritus Seiji Tobita for fruitful discussions. The ^1H -NMR spectral measurements were performed using a JNM-ECS400 (JEOL) operated at 400 MHz at the Center for Instrumental Analysis of Gunma University.

Author contributions

T.Y., T.T., and S.S. designed the experiments. T.T., S.S., L.C., and R.K. carried out the experiments. T.Y., T.T., and S.R. wrote the manuscript. All authors reviewed the manuscript.

Competing interests

The authors declare no competing interests.

Additional information

Supplementary Information The online version contains supplementary material available at <https://doi.org/10.1038/s41598-024-69369-5>.

Correspondence and requests for materials should be addressed to T.Y.

Reprints and permissions information is available at www.nature.com/reprints.

Publisher's note Springer Nature remains neutral with regard to jurisdictional claims in published maps and institutional affiliations.

Open Access This article is licensed under a Creative Commons Attribution-NonCommercial-NoDerivatives 4.0 International License, which permits any non-commercial use, sharing, distribution and reproduction in any medium or format, as long as you give appropriate credit to the original author(s) and the source, provide a link to the Creative Commons licence, and indicate if you modified the licensed material. You do not have permission under this licence to share adapted material derived from this article or parts of it. The images or other third party material in this article are included in the article's Creative Commons licence, unless indicated otherwise in a credit line to the material. If material is not included in the article's Creative Commons licence and your intended use is not permitted by statutory regulation or exceeds the permitted use, you will need to obtain permission directly from the copyright holder. To view a copy of this licence, visit <http://creativecommons.org/licenses/by-nc-nd/4.0/>.

© The Author(s) 2024